

## Supporting information

### Comparison of Liquid Exfoliated Transition Metal Dichalcogenides Reveals MoSe<sub>2</sub> to be the Most Effective Hydrogen Evolution Catalyst

Zahra Gholamvand,<sup>1,2</sup> David McAteer,<sup>1,2</sup> Claudia Backes,<sup>1,2</sup> Niall McEvoy,<sup>1,3</sup> Andrew Harvey,<sup>1,2</sup> Nina C. Berner,<sup>1, 3</sup> Damien Hanlon,<sup>1,2</sup> Conor Bradley,<sup>1</sup> Ian Godwin,<sup>1,2</sup> Aurlie Rovetta,<sup>1,3</sup> Michael Lyons,<sup>1,3</sup> Georg S. Duesberg,<sup>1,3</sup> and Jonathan N. Coleman<sup>1,2\*</sup>

<sup>1</sup>CRANN & AMBER, Trinity College Dublin, Dublin 2, Ireland

<sup>2</sup>School of Physics, Trinity College Dublin, Dublin 2, Ireland

<sup>3</sup>School of Chemistry, Trinity College Dublin, Dublin 2, Ireland

colemaj@tcd.ie

## Experimental Detail

### Materials

All starting powders were >99% pure and purchased in powder form. For each material, supplier and particle sizes were as follows: MoS<sub>2</sub> (Sigma Aldrich, <2 μm), MoSe<sub>2</sub> (Materion, <45 μm), MoTe<sub>2</sub> (Materion, <10 μm), WS<sub>2</sub> (Sigma Aldrich, <2 μm), WSe<sub>2</sub> (Materion, <5 μm) and WTe<sub>2</sub> (American Elements). Arc-discharge purified single-walled carbon nanotube SWNT powder was purchased from Iljin Nanotech Co. Sodium cholate hydrate (NaC) were purchased from Sigma Aldrich at the highest available purity and used as received.

### Preparation of exfoliated TMDs dispersion

For this current study all the S and Se compounds were exfoliated with the same protocol and the two tellurides (MoTe<sub>2</sub> and WTe<sub>2</sub>) were prepared with a few modifications. Typically, MX<sub>2</sub> dispersions (M=Mo, W and X=S, Se) were prepared by probe sonicating (Heilsher model UP200S, 200 W, 24 kHz) the starting powder (Ci=20 mg mL<sup>-1</sup>) in 70 mL of aqueous sodium cholate solution (C<sub>NaC</sub>=6 mg mL<sup>-1</sup>). Worth noting that the weight ratio of NaC to TMD powder initial concentration was kept 0.3 which is the optimized concentration of the surfactant in order to drive efficient exfoliation, obtain stable nano-sheet dispersion and avoid re-stacking. The initial dispersion was sonicated for 6 hours at 60% amplitude in pulsed mode with 4 s on 1 s off while chilled using double jacketed water cooling system and chiller. The resultant raw dispersions were subjected to a brief centrifugation step (Hettich Mikro 22R centrifuge) at 1500 RPM (240 g) for 90 minutes to remove un-exfoliated material. Then the concentration of the decanted supernatant was determined gravimetrically after filtering certain volume of the dispersions onto alumina membranes (pore size 20 nm) and post-washing the films with 600 mL of water each to remove residual surfactant. The membranes with as-filtered TMDs were dried in vacuum at 60°C overnight and the deposited mass per filtered volume was used to determine each dispersion's concentration.

In the case of MoTe<sub>2</sub> and WTe<sub>2</sub>, suspensions were prepared by adding 350 mg of TMD powder (Ci=5 mg mL<sup>-1</sup>) to 70 ml of sodium cholate solution and sonicating for 3 hours at 60% amplitude in pulsed mode with 4 s on 4 s off.

### Preparation of Carbon nanotube dispersions

Arc-discharge single-walled carbon nanotube powder (SWNTs, IJin Nanotech Co.) was used as a conductor. In order to make highly de-bundled SWCNT dispersion, 50 mg CNT powder was added to 50 ml of 10 mg mL<sup>-1</sup> aqueous sodium cholate stock solution such that the surfactant to CNT mass ratio in the resultant dispersions was 10:1 (SWNT Ci= 1 mg mL<sup>-1</sup>). The total volume was divided into 15 ml vials and each vial was subjected to 5 minutes of high power tip sonication (VibraCell CVX; 750W, 60 kHz, 20% amplitude) then 30 min of bath sonication (Branson 1510-MT sonic bath, 20 kHz), followed by another 5 minutes of tip sonication and 1 hour bath sonication. The black dispersions were then centrifuged at 5500 rpm for 90 minutes and the supernatant of each dispersion was carefully decanted and combined. The final concentration was calculated by measuring the absorbance (PerkinElmer 650 spectrometer) of 25 time diluted dispersion at 660 nm and using the Lambert-Beer law, knowing the extinction coefficient of the SWNT (3389 mL/mg/m at 660 nm). All the dispersions were stored in a refrigerator for further use.

### ***Electrode Preparation***

Based on the concentration of TMD nano-sheets in each dispersion, precise volumes were extracted in order to make films with a desire mass per area (0.1 mg/cm<sup>2</sup> and 1 mg/cm<sup>2</sup>) and vacuum-filtered onto porous cellulose filter membranes (MF-Millipore membrane, mixed cellulose esters, hydrophilic, 0.025 μm) to give uniform films. To make TMD/SWNT composite films known volumes of TMD dispersions were pipetted into a vial and mixed with 10 wt% of dispersed SWNTs and put in a sonic bath for 10 min and then vacuum filtered. The deposited films were then cut into pieces (~0.65 cm<sup>2</sup>) and transferred on pyrolytic carbon (PyC) electrodes via previously reported transferring method. The cellulose filter membrane was then removed by treatment with acetone vapour and subsequent acetone liquid baths followed by isopropanol rinse to remove the acetone residual. The typical process of making electrodes from a dispersion to the final catalyst electrodes is depicted in Figure S- 1 schematically.

Pyrolytic carbon was grown by chemical vapour deposition (CVD) from an acetylene feedstock at 950 °C for 30 min to a thickness of 300–400 nm on 300 nm thermally deposited SiO<sub>2</sub> on Si substrates in a hot wall quartz tube furnace as previously reported.

### ***The substrate selection to support TMD films***

The initial challenge for evaluating the HER activity of TMDs accurately was choosing an appropriate electrochemically inert electrically conductive substrate which exhibits no electrochemical activity under the testing conditions and stays stable between 0 to -0.8 V vs RHE. We opted pyrolytic carbon electrode over glassy carbon disc electrode for few reasons. First of all it is a very convenient type of electrode which saves a lot of time because there is no need for polishing or any pre or post preparation, so many electrode can be prepared and tested at the same time. Therefore the results are quite reproducible, not affected by aging and are not dependant on the polishing quality of the support. Secondly because of the plate shape of the electrodes they can be set up the way that the surface of the electrode is observable during the HER test so that the any changes in electrodes such as damage or bubbling out can be controlled visually. This is very important to avoid relating any difference in HER performance to the type of material which is actually arising from crack or losing catalyst due to vigorous hydrogen bubbling (Figure S-1B). With this type of electrodes time consuming experiments on failed films can be avoided. Because the final electrodes are plate like so can be set up in

parallel geometry as shown in Figure S-3 which helps the H<sub>2</sub> bubbles to slide up away from the surface of the electrolyte by the gravity force without sticking to the catalyst and blocking the catalyst surface which cause current drift (Figure S-1C). Therefore it was possible to do experiments without rotating disc electrode (RDE) instrument. In addition PyC flat current collector offers very precise control over mass and thickness of the catalyst which makes it possible to compare actual HER activity of different TMDs accurately as well as SWNTs percolation for future studies. The most important advantages of PyC over other flat conductive electrodes is being quite inert in desired experimental potential window and stable which does not change by voltage and time (Figure S1-A) thus provides accurate data which current can be only contributed to the catalytic activity of the active material.

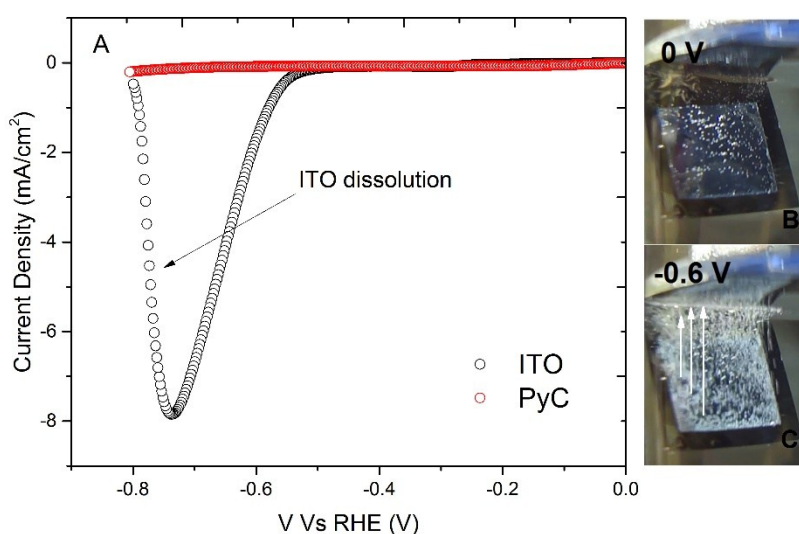


**Figure S- 1:** Linear sweep voltammetry of bare PyC against bare ITO within experimental potential window in 0.5M H<sub>2</sub>SO<sub>4</sub> electrolyte. This shows in this voltage range PyC is quite inert with only a small current (few micro-ampere) passing through the substrate in voltages higher than 700 mV. However ITO not only generate considerable amount of current in potential higher than 500 mV (maximum current of 7 mA/cm<sup>2</sup> at 700 mV) but also dissolves at potential higher than 750 mV until current reach zero

### ***Film characterisation***

Small pieces of each film were transferred on double frosted glass slide using the same method for thickness measurement and electrical conductivity measurements. Film thickness was measured by profilometry using a Dektak 6M, Veeco Instruments. Step profiles were obtained at three locations on the film and averaged. Electrical conductivity values were calculated from resistivity measurements made using a four-point probe technique with a Keithley 2400 source meter (Keithley Instruments, Inc.) with LabView interface (National Instruments, Inc.). Silver electrodes were attached to the films and the film width and electrode separations were carefully recorded. Conductivity of the films were calculated from Equation S-1 where R is calculated resistance from Ohm's law, L is electrode separation length, W is film width and t is the thickness measured by profilometer.

Eq S- 1

$$R = \frac{1}{\sigma_{DC}} \frac{L}{Wt}$$

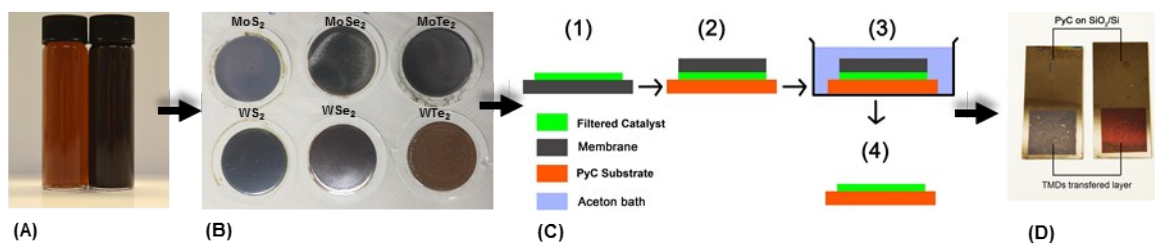


**Figure S-2:** Schematic illustration of electrode preparation for electrochemical measurements. (A) Calculated volumes of each dispersion (with and without SWNTs) were filtered to make TMD and 10% SWNT films with desired M/A shown in (B). (C) The transfer process to deposit catalyst onto the PyC current collector. (D) Final electrodes with the desired M/A on PyC electrode ready for the electrochemical measurements.

## Material Characterisation methods

### *UV/Vis*

Optical extinction was measured on a Perkin Elmer 1050 spectrometer in quartz cuvettes with a path length of 0.4 cm. The dispersions were diluted by aqueous surfactant solution immediately prior to the measurement to yield optical densities below 1.5. To differentiate contributions from scattering and absorbance to the extinction spectrum, the dispersion was measured in an integrating sphere using a home-built sample holder to place the cuvette in the centre of the sphere of a Perkin Elmer Lambda 650 spectrometer (NB cuvettes need to be transparent to all sides). The absorbance spectrum is obtained from the measurement inside the sphere and the scattering spectrum was calculated by subtracting these two spectrum (extinction-absorbance). From each measurement, the respective baseline of surfactant solution was subtracted.

### *TEM*

Bright field transmission electron microscopy imaging was performed using a JEOL 2100, operated at 200 kV. Holey carbon grids (400 mesh) were purchased from Agar Scientific and samples were prepared by diluting dispersion to a low concentration and drop casting onto a grid placed on filter paper to wick away excess surfactant/water. Statistical analysis was performed of the flake dimensions by measuring the longest axis of the nano-sheet and assigning it “length” for 100 flakes and averaging them.

### *Raman*

Raman spectra were acquired using a Witec Alpha 300 R with a 532 nm excitation wavelength and 1800 lines/mm grating. Representative spectra for each material were obtained by averaging line scans consisting of 50 discrete point spectra. Low laser powers (< 100 uW) were used in order to minimise sample damage.

### *XRD*

Powder XRD was performed using a Siemens D500 X-ray Diffractometer equipped with a  $\text{Cu}_{K\alpha}$  emission source ( $\lambda = 1.54056 \text{ \AA}$ ) filtered through a graphite monochromator at ambient temperature. Data were collected in 0.02 degree steps with scan rate of 3 seconds per step.

XRD samples were made by filtering dispersion onto alumina membrane to form thick films. Data were analysed by Bruker EVA software.

### ***XPS***

X-ray Photoelectron Spectroscopy was performed under ultra-high vacuum conditions ( $<5 \times 10^{-10}$  mbar), using monochromated Al K $\alpha$  X-rays (1486.6 eV) from an Omicron XM1000 MkII X-ray source and an Omicron EA125 energy analyzer. The analyzer pass energy was set to 100 eV for survey and 20 eV for core-level spectra, yielding a maximum energy resolution of  $\sim 0.65$  eV. An electron flood gun was used for charge compensation and the binding energy scale was referenced to the adventitious carbon 1s core-level at 284.8 eV. After subtraction of a Shirley background, the core-level spectra were fitted with Gaussian–Lorentzian line shapes.

### ***SEM***

Scanning electron microscopy was performed on electrodes before and after HER test using Carl Zeiss Ultra microscope operated at 5 kV to acquire the secondary electron images of sample.

### **Electrochemical characterisation**

All the electrochemical measurements were performed in 0.5 M H<sub>2</sub>SO<sub>4</sub> solution using a three-electrode cell, with an Ag/AgCl (3 M NaCl) reference electrode and graphite rod counter electrode. Electrochemical tests consisted of linear sweep voltammetry and electrochemical impedance spectroscopy using Gamry Reference 3000 potentiostat. The measured potential was converted to the RHE scale by adding +0.210 V, measured with respect to a Gaskatel Hydroflex H<sub>2</sub> reference electrode. The electrocatalysis was measured using linear sweeping from 0 V to -0.9 V (vs. RHE) with a scan rate of 5 mV/s. The AC impedance is measured within the frequency range of 0.1 to 10<sup>5</sup> Hz with perturbation voltage amplitude of 10 mV and different DC potential bias. The equivalent series resistance of the system was measured by impedance spectroscopy from the high frequency intercept with the real impedance axis and all the data were corrected by iR compensation. We note that, because of the parallel combination of capacitance and resistance representing the electrode, iR compensation only removed the effects of the electrolyte and not the electrode. Cyclic voltammograms were recorded by cycling each samples 10 times between 0 to +0.4 V vs RHE. The stability of the samples were tested using Chronoamperometric method which is holding each electrode in fixed potential (-0.4 V vs RHE) for certain amount of time and measuring current versus time.

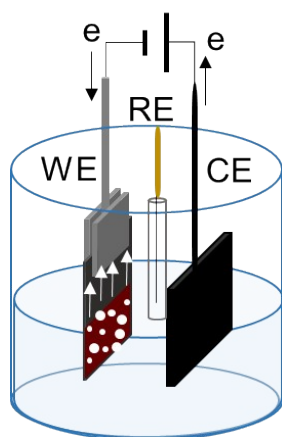


**Figure S- 3:** Schematic of HER working electrode vertical geometry. Working electrode with deposited catalyst film (WE), Ag/AgCl reference electrode (RE) and graphite plate counter electrode (CE). The geometry of the electrode helps the H<sub>2</sub> bubbles to slide away from the surface to the electrolyte due to gravity and made it possible to do experiments without a rotating electrode device. The other advantages of this geometry is that any failure of the films can be observed to avoid time consuming experiments on damaged films.

## Results

### *XRD patterns of MoSe<sub>2</sub> raw powder and exfoliated films*

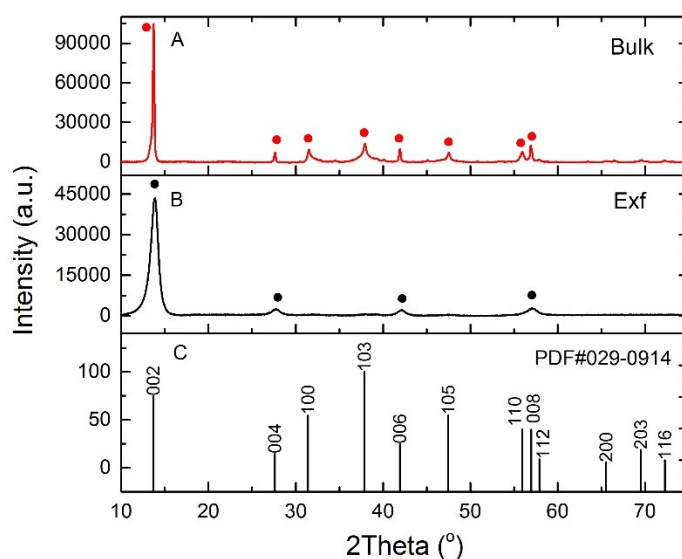


**Figure S-4:** XRD pattern of (A) MoSe<sub>2</sub> bulk powder comparing to (B) exfoliated MoSe<sub>2</sub> and corresponding (C) reference pattern of crystalline MoSe<sub>2</sub>. When periodicity in the c-axis is present in bulk materials, a strong (002) peak is usually observed at a value of 2θ around 14° in contrast, this signal should not detect in single layer TMDs. The lower intensity of (002) plane peak in exfoliated sample comparing to the bulk confirms the presence of few layer MoSe<sub>2</sub> nanosheets and (002) peak broadening shows decreased lateral flake size. Note that because the MoSe<sub>2</sub> nanosheets lie on the substrate with preferred orientation, in principle, the peaks except that for (002) plane are not observable in films made of exfoliated nanosheets. In both bulk and exfoliated MoSe<sub>2</sub> the crystal structure can be indexed to pure 2H-MoSe<sub>2</sub> with no sign of additional oxides.

### Characterisation of MoS<sub>2</sub> bulk and exfoliated MoS<sub>2</sub> nanosheets

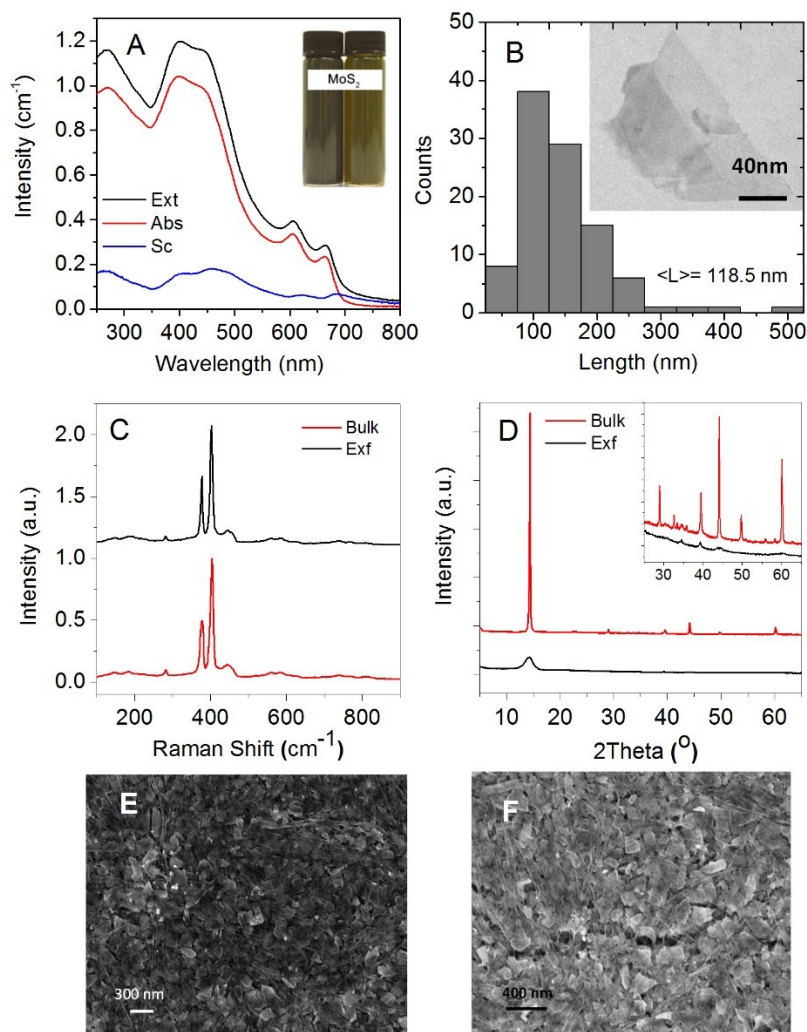


**Figure S-5:** (A) Optical extinction, absorbance and scattering spectra of MoS<sub>2</sub> nano-sheet dispersion in Water/SC. Inset: Photograph of standard MoS<sub>2</sub> dispersion (left vial) and 40 times diluted dispersion. (B) Transmission electron microscopy size histogram of 100 MoS<sub>2</sub> counted flakes showing the average flake size of 118 nm. Inset: Representative low-resolution bright field TEM images of MoS<sub>2</sub> nanosheets exfoliated in Water/SC. (C) Raman spectrum of the source MoS<sub>2</sub> powder and exfoliated nanosheets showing the characteristic peaks at 380, 408, and 455 cm<sup>-1</sup> of  $E_{2g}^1$ ,  $A_{1g}$ , and longitudinal acoustic phonon modes of 2H-MoS<sub>2</sub>, respectively. (D) XRD of MoS<sub>2</sub> powder and MoS<sub>2</sub> exfoliated filtered film can be indexed to pure crystalline 2H-MoS<sub>2</sub> prior and after exfoliation. The considerable decreased intensity and broadening of the (002) peak at 2θ of 14° after exfoliation is being consistent with decreased lateral size of few layer MoS<sub>2</sub> nanosheets. (E, F) SEM images of the as prepared electrodes (catalyst film transferred on PyC) before HER test: (E) SEM image of MoS<sub>2</sub> film (F) SEM image of MoS<sub>2</sub>/SWNTs composite film

### Characterisation of WS<sub>2</sub> bulk and exfoliated WS<sub>2</sub> nanosheets

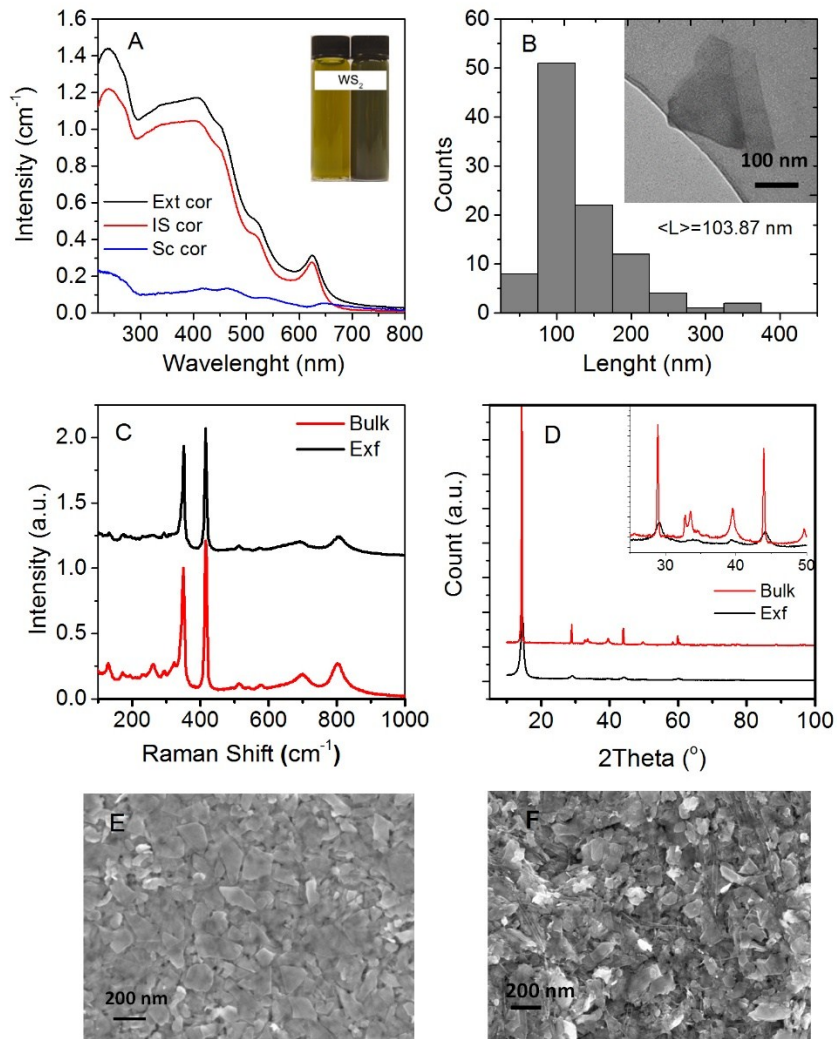


**Figure S-6:** (A) Optical extinction, absorbance and scattering spectra of WS<sub>2</sub> nano-sheet dispersion in Water/SC. Inset: Photograph of standard WS<sub>2</sub> dispersion (left vial) and 50 times diluted dispersion. (B) Transmission electron microscopy size histogram of 100 WS<sub>2</sub> counted flakes showing the average flake size of 104 nm. Inset: Representative low-resolution bright field TEM images of WS<sub>2</sub> nanosheets exfoliated in Water/SC. (C) Raman spectrum of the source WS<sub>2</sub> powder and exfoliated nano-sheets showing the characteristic phonon modes of 2LA(M) $E_{2g}^1$  and  $A_{1g}$  at 350 and 419 cm<sup>-1</sup> respectively with some additional peak at 697 and 803 cm<sup>-1</sup> which matches with vibration modes of WO<sub>3</sub>. (D) XRD of WS<sub>2</sub> powder and WS<sub>2</sub> exfoliated filtered film matches the crystal structure of WS<sub>2</sub> with some signs of WO<sub>3</sub> oxide in bulk WS<sub>2</sub> powder at 2θ of 32° and 34° correspond to (022) and (202) plane of WO<sub>3</sub> which decreased considerably after exfoliation due to film post processing. (E, F) SEM images of the as prepared electrodes (catalyst film transferred on PyC) before HER test: (E) SEM image of WS<sub>2</sub> film (F) SEM image of WS<sub>2</sub>/SWNTs composite film

## Characterisation of WSe<sub>2</sub> bulk and exfoliated WSe<sub>2</sub> nanosheets

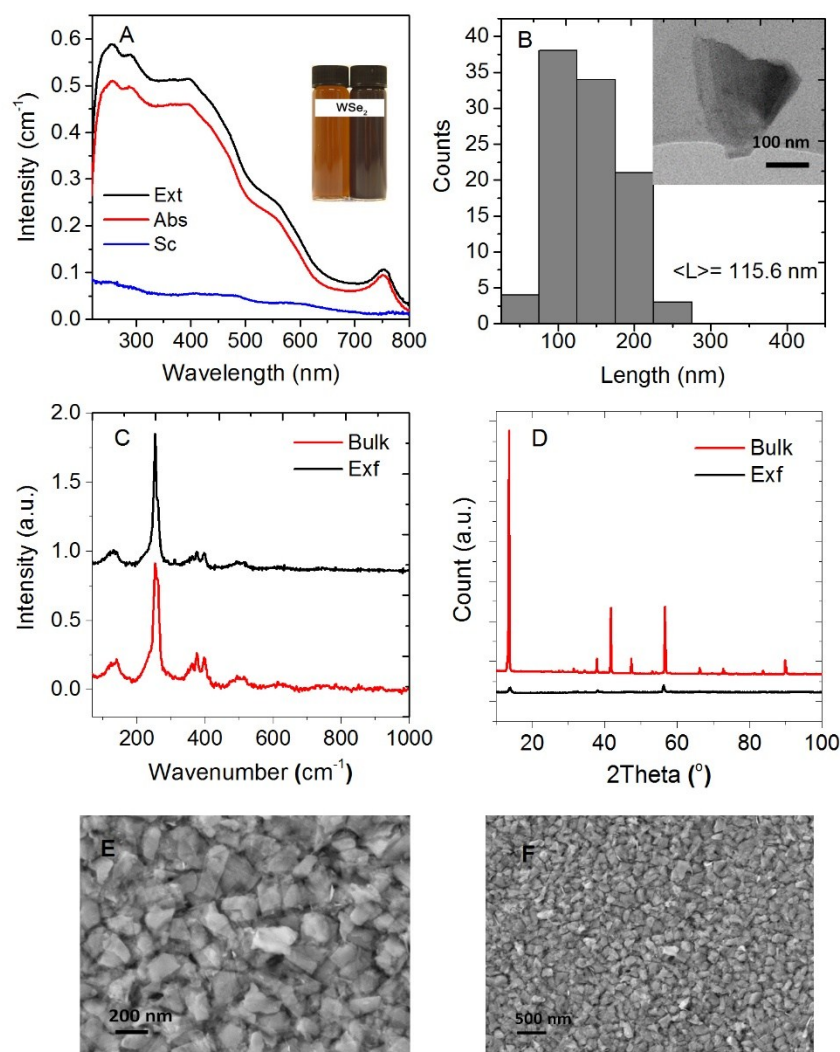


**Figure S-7:** (A) Optical extinction, absorbance and scattering spectra of WSe<sub>2</sub> nano-sheet dispersion in Water/SC. Inset: Photograph of standard WSe<sub>2</sub> dispersion (left vial) and 80 times diluted dispersion. (B) Transmission electron microscopy size histogram of 100 WSe<sub>2</sub> counted flakes showing the average flake size of 115 nm. Inset: Representative low-resolution bright field TEM images of WSe<sub>2</sub> nanosheets exfoliated in Water/SC. (C) Raman spectrum of the source WSe<sub>2</sub> powder and exfoliated nano-sheets showing the characteristic phonon modes of  $E_{2g}^1$  and  $A_{1g}$  at 248 and 250 cm<sup>-1</sup> respectively often manifest as one peak due to overlapping. No obvious sign of oxides can be distinguished in Raman spectra. (D) XRD of WSe<sub>2</sub> powder and exfoliated WSe<sub>2</sub> filtered film is in accordance with pure crystalline WSe<sub>2</sub> prior and after exfoliation. The considerable decreased intensity and broadening of the (002) peak at  $2\theta$  of 14° after exfoliation shows considerable decrease in lateral size of few layer thin WSe<sub>2</sub> nanosheets. (E, F) SEM images of the as prepared electrodes before HER test: (E) SEM image of WSe<sub>2</sub> film (F) SEM image of WSe<sub>2</sub>/SWNTs composite film

## Characterisation of MoTe<sub>2</sub> bulk and exfoliated MoTe<sub>2</sub> nanosheets

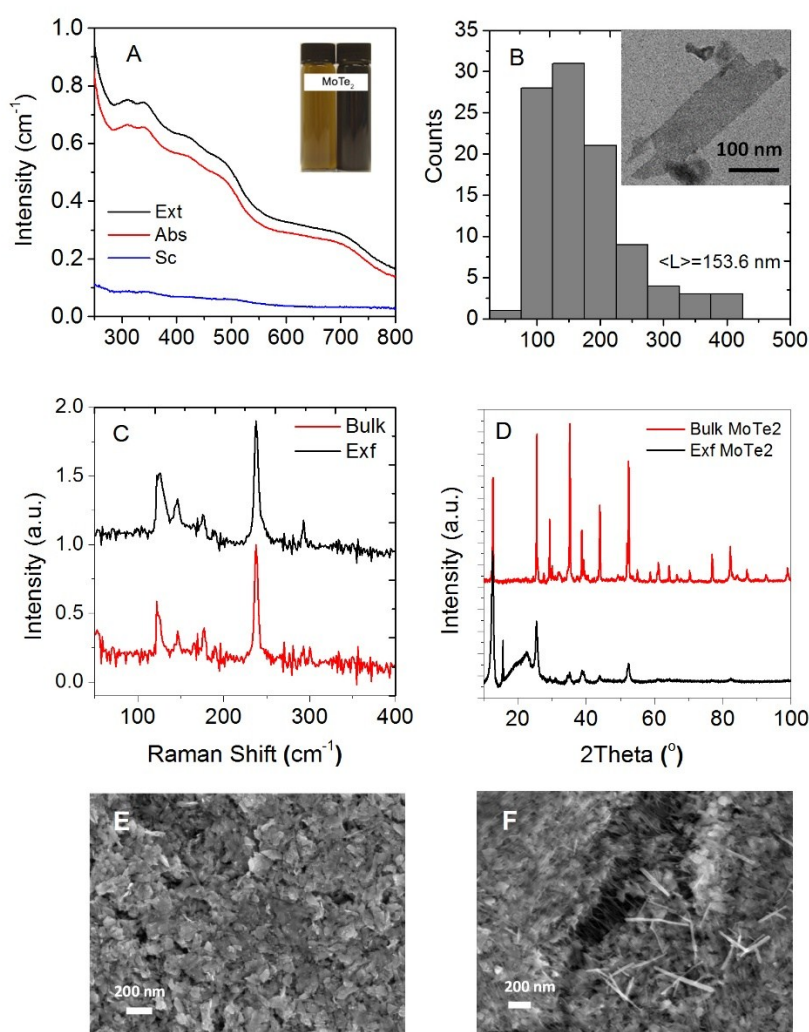


**Figure S-8:** (A) Optical extinction, absorbance and scattering spectra of MoTe<sub>2</sub> nano-sheet dispersion in Water/SC. Inset: Photograph of standard MoTe<sub>2</sub> dispersion (left vial) and 20 times diluted dispersion. (B) Transmission electron microscopy size histogram of 100 MoTe<sub>2</sub> counted flakes showing the average flake size of 153 nm. Inset: Representative low-resolution bright field TEM images of MoTe<sub>2</sub> nano-sheets exfoliated in Water/SC shows that MoTe<sub>2</sub> have relatively rough surface which looks like very small particles sitting all over the flake basal plane. This is likely oxides from MoTe<sub>2</sub> oxidation into MoO<sub>3</sub> or TeO<sub>2</sub> by aging the sample. (C) Raman spectrum of the source MoTe<sub>2</sub> powder and fresh exfoliated MoTe<sub>2</sub> film represents the characteristic phonon modes of  $E_{2g}^1$  and  $B_{2g}^1$  at 238 and 293 cm<sup>-1</sup> respectively. The other peaks at 125 and 144 cm<sup>-1</sup> are likely correspond to tellurium oxide. (D) XRD of MoTe<sub>2</sub> powder and exfoliated filtered MoTe<sub>2</sub> film also confirms some amount of oxides. (E) SEM image of the as prepared MoTe<sub>2</sub> catalyst film transferred on PyC before HER test. (F) SEM image of MoTe<sub>2</sub>/SWNTs composite film. SEM images also confirms the oxidation of MoTe<sub>2</sub> nano-sheets which results in round edge shaped flakes instead of sharp edges. More oxide can be clearly seen in image (F) as white needle-like shape which is more likely  $\alpha$ -TeO<sub>2</sub>.

## Characterisation of $WTe_2$ bulk and exfoliated $WTe_2$ nanosheets

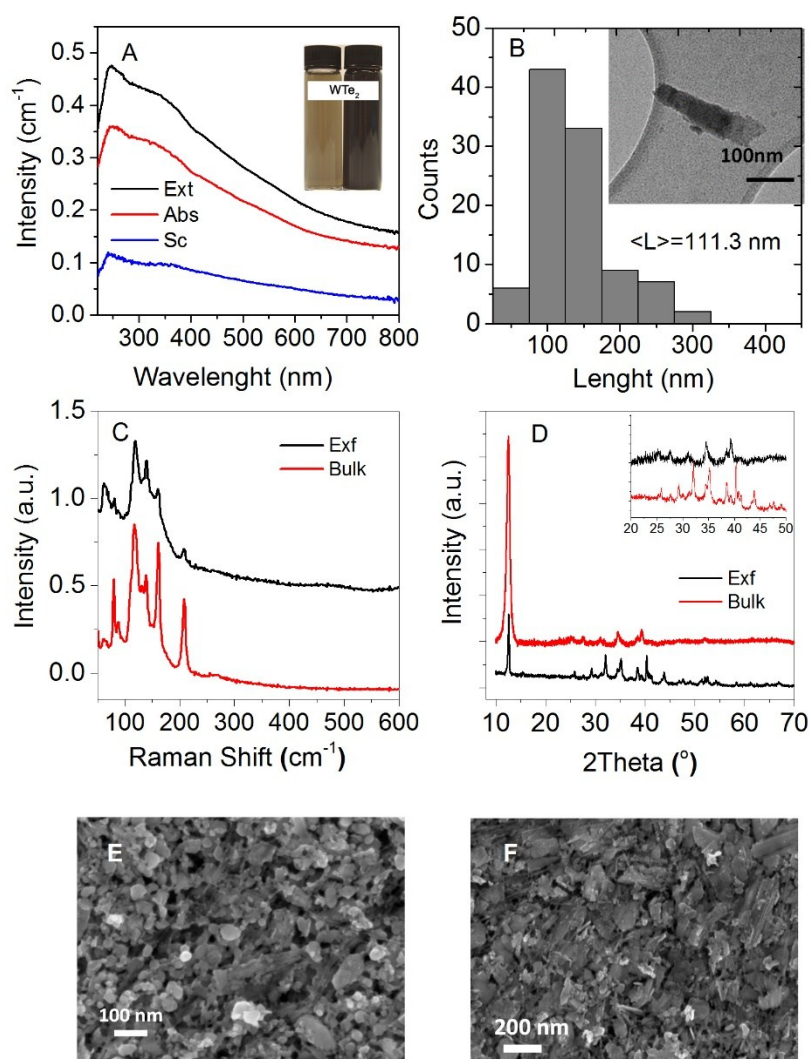


**Figure S- 9:** (A) Optical extinction, absorbance and scattering spectra of a  $WTe_2$  nano-sheet dispersion in Water/SC. Inset: Photograph of standard  $WTe_2$  dispersion (left vial) and 30 times diluted dispersion. (B) Transmission electron microscopy size histogram of 100  $WTe_2$  counted flakes showing the average flake size of 111 nm. Inset: Representative low-resolution bright field TEM images of  $WTe_2$  nano-sheets exfoliated in Water/SC shows dissolution of the flakes. (C) Raman spectrum of the source  $WTe_2$  powder and exfoliated  $WTe_2$  film represents some additional peaks to characteristic peaks at 160 and  $\sim 207$   $cm^{-1}$  which are consistent with  $TeO_2$  and  $WO_3$  as confirmed by XPS analysis. (D) XRD of  $WTe_2$  powder and exfoliated filtered  $WTe_2$  film confirms large amount of oxides present on both starting powder and processed exfoliated  $WTe_2$  film. (E) SEM image of the as prepared  $WTe_2$  film transferred on PyC before HER test. (F) SEM image of  $WTe_2$ /SWNTs composite film. SEM images shows that exfoliated  $WTe_2$  looks more like round particles than nano-sheets which also confirms degradation and oxidation of  $WTe_2$  nano-sheets to other phases such as  $TeO_2$  and  $WO_3$ .

### *XRD patterns of pure TMDs single crystalline reference*

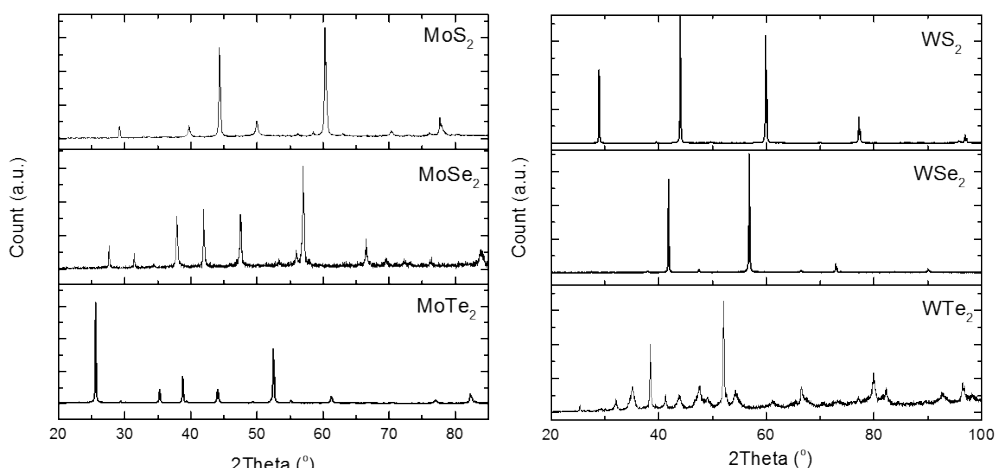


**Figure S-10:** XRD patterns of standard single crystalline TMDs

### *Polytype*

As confirmed by Raman, XRD and UV/vis spectra, all the materials maintain their 2H during at all stages without undergoing any phase transition from 2H to 1T either during liquid phase exfoliation or HER.

### *Stability of TMDs before and after HER test*

One important characteristic of a good catalyst is being stable against oxidation in order to have efficient life-time. We characterised each TMDs powder as precursor, after exfoliation (before electrochemical HER test) and after HER, to be able to correlated the HER activity to the quality of the material and also to find out which catalyst is stable under experimental condition for HER application. As confirmed by Raman, XRD and UV/vis spectra, all the materials maintain their 2H during the process without undergoing any phase transition from 2H to 1T after liquid phase exfoliation.

As previously shown MoSe<sub>2</sub> is the most stable TMD with the highest HER activity which shows no sign of oxide even after HER cycling. However MoTe<sub>2</sub> and WTe<sub>2</sub> are showing the highest amount of oxides in both starting powder and processed exfoliated films which makes them not attractive material for HER application in contrast with their relatively high electrical conductivity. Figure S-11 shows the XPS spectra of as-prepared WTe<sub>2</sub> electrode before and after HER experiment as the poorest catalyst amongst the selected TMDs. In contrast with Tellurides, Sulphides and selenides are quite stable under experimental condition. Raman spectra of MoS<sub>2</sub> electrodes before and after HER cycling test shown in Figure S-12 confirms the absence of oxides even after 30 min of chronoamperometric test. Raman map of  $A_{1g}$  peaks before HER (B) and after HER (C) shows similar intensity and confirms the homogeneity of the films after HER test.

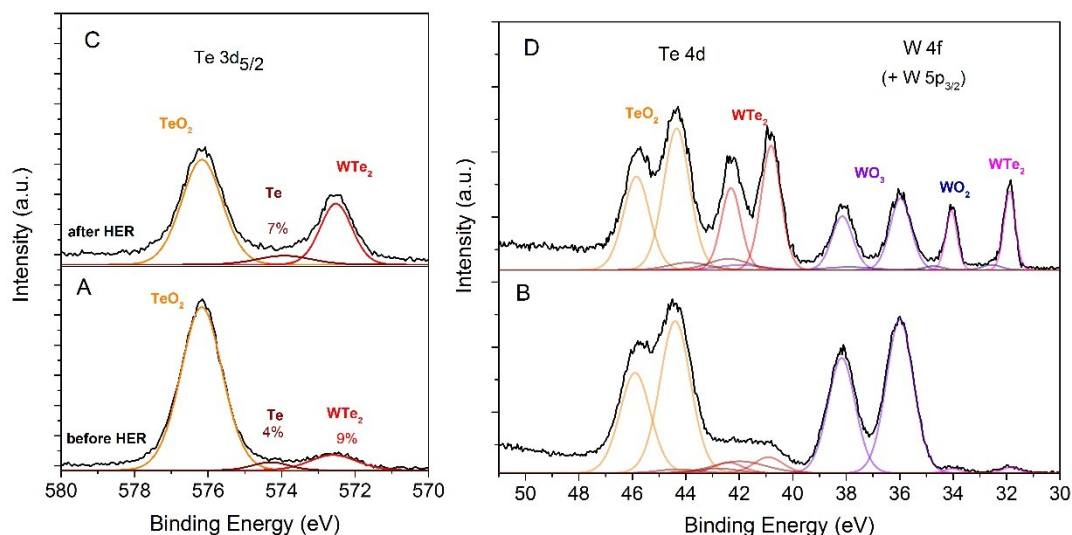


**Figure S-11:** XPS spectra of WTe<sub>2</sub> electrodes (A, B) before and (C, D) after HER shows that more than 85% of TeO<sub>2</sub> oxide are present in WTe<sub>2</sub> before HER test. Therefore the poor performance of WTe<sub>2</sub> can be related to the oxidation of WTe<sub>2</sub>

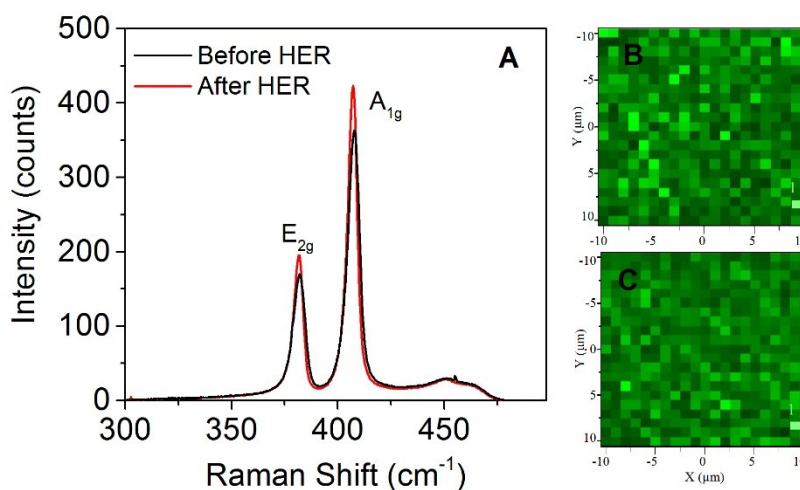


**Figure S- 12:** (A) Raman spectra of MoS<sub>2</sub> electrode before and after HER. (B, C) Raman map of  $A_{1g}$  mode shows similar intensity in both samples and homogeneous distribution all over the electrode.

### **SEM images of composite films before and after HER**

In order to examine the integrity of the electrodes during the HER test and the effect of electrochemical process on morphology of the nano-sheets, SEM images of as-prepared electrodes were collected (shown in characterisation figures of each material in Figure S-5 to Figure S- 9) and compared with the SEM images of the electrode's surfaces after HER shown in Figure S-13 and Figure S-14. Similar to as-prepared electrodes (via filtration/ wet-transfer) , Mo and W sulphide and selenide films are homogenous over long length-scales after HER test and they consist of disordered arrays of nano-sheets with clear and sharp edges over short length-scales. However some white needle-like rods can be recognised all over the surface of MoTe<sub>2</sub> and WTe<sub>2</sub> films which is found to be tellurium oxide from XPS analysis (Figure S-1).

These films are also mechanically weak and cracked which can be related to formation of oxide deep in profile and not only on the surface.  $\text{WTe}_2$  films shows the most significant alteration after HER test. In addition to  $\text{TeO}_2$  rods all over the surface  $\text{WTe}_2$  nano-sheets could not be distinguished clearly. This might be due to the complete dissolution of the flakes into oxide as shown in Figure S-14 (E and F).

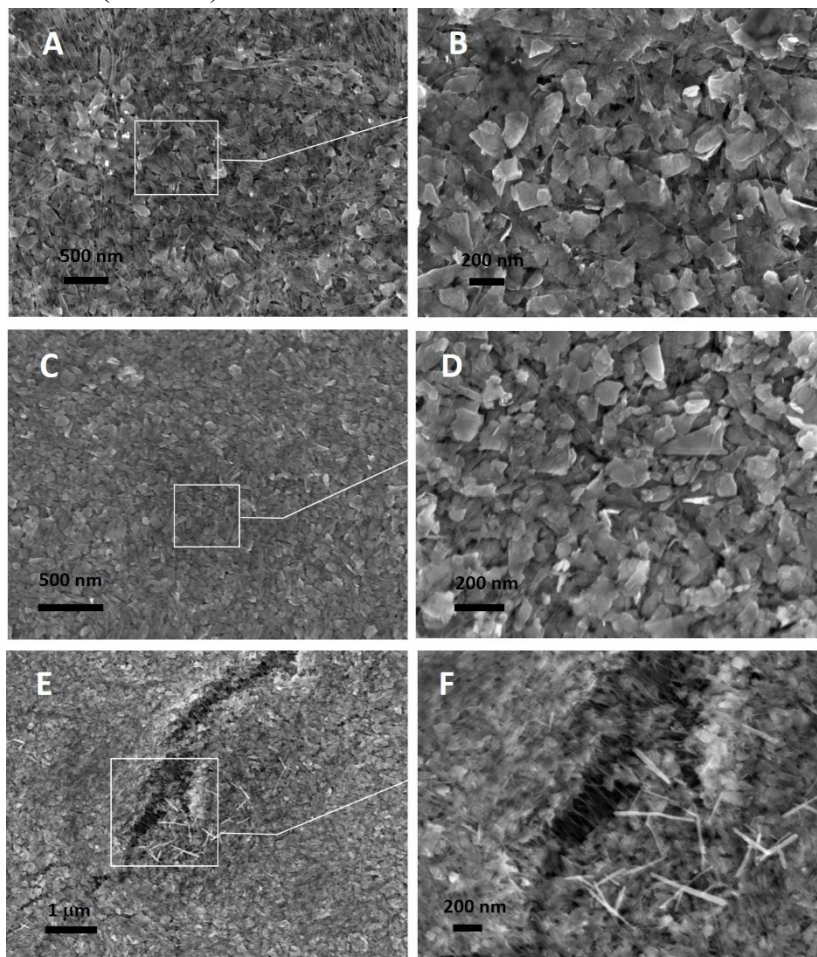


**Figure S- 13:** SEM images of Molybdenum TMDs after HER experiments.  $\text{MoS}_2$  (A, B),  $\text{MoSe}_2$  (C, D),  $\text{MoTe}_2$  (E, F)

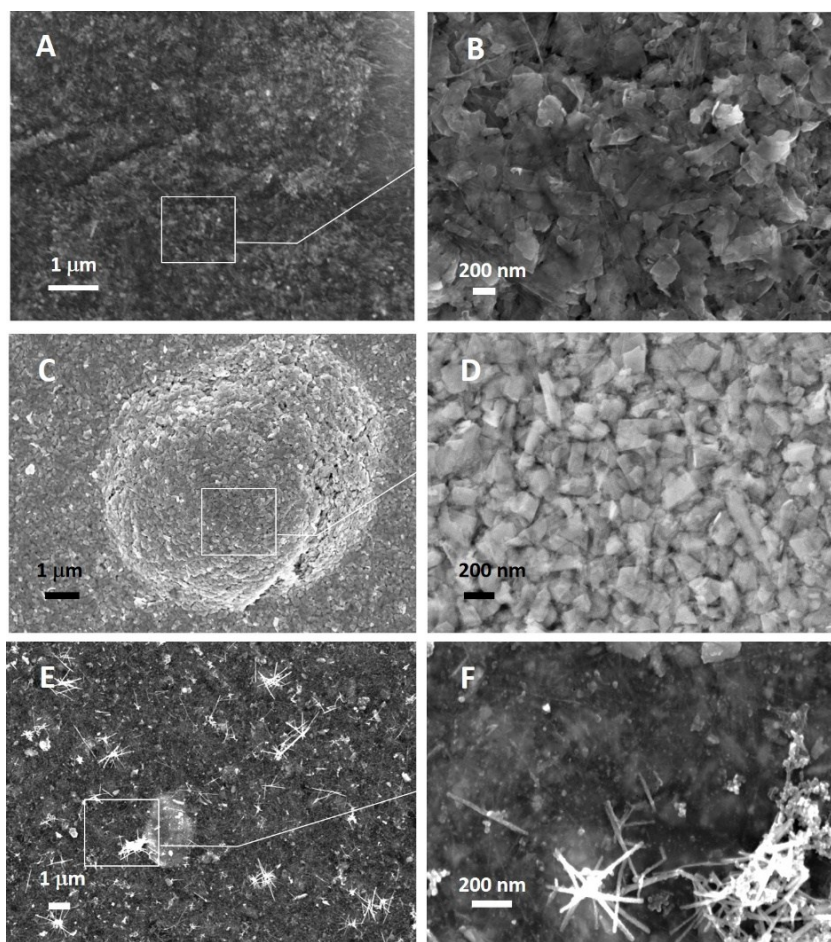
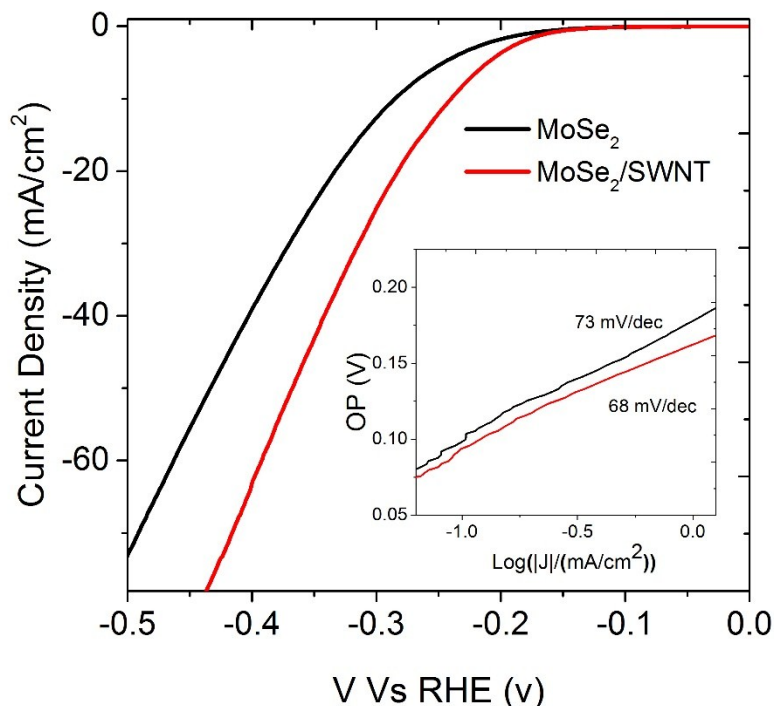


**Figure S- 14:** SEM images of Tungsten TMDs after HER. WS<sub>2</sub> (A, B), WSe<sub>2</sub> (C, D), WTe<sub>2</sub> (E, F)

**Effect of adding SWNTs on thin and thick MoSe<sub>2</sub> films**



Parameter	0.1 mg/cm <sup>2</sup>		0.5 mg/cm <sup>2</sup>	
	MoSe <sub>2</sub>	MoSe <sub>2</sub> /SWNT	MoSe <sub>2</sub>	MoSe <sub>2</sub> /SWNT
TS (mV/dec)	76	71	73	68
J <sub>0</sub> (μA/cm <sup>2</sup> )	1.9	1.7	3.9	3.8
Onsetpotential (V)	205	196	179	163
η for 10 mA/cm <sup>2</sup>	288	276	285	240

**Figure S-15:** Polarisation curves of 0.5 mg/cm<sup>2</sup> MoSe<sub>2</sub> and MoSe<sub>2</sub>/SWNT 10wt% with the corresponding Tafel plots (inset graph). Summary table of extracted data from pure MoSe<sub>2</sub> and composite films with low mass loading (0.1 mg/cm<sup>2</sup>) comparing the high mass loading (0.5 mg/cm<sup>2</sup>). For both mass loadings adding SWNT conductors reduces the Tafel slope by 5 mV/dec where exchange current density did not change considerably. Also onset potential decreased 9 mV and 14 mV for low and high mass loading respectively. The difference in overpotential required to generate 10 mA/cm<sup>2</sup> current for pure MoSe<sub>2</sub> films and composite film is much larger for the thicker film (45 mV/dec) comparing the thinner film (12 mV). This can confirm that the addition of the conductor in high mass loading can effectively enhance the catalytic activity by overcoming the charge transfer limited by the conductivity of the thick films

### Cyclic voltammograms of TMD films and their corresponding double layer capacitance

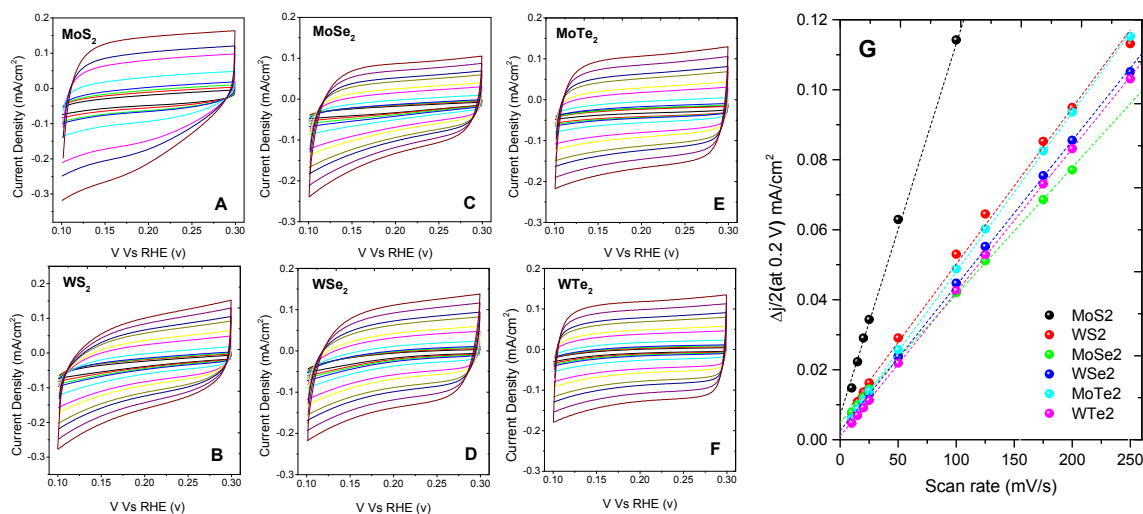


**Figure S-16:** Electrochemical double-layer capacitance measurements. (A-F) Cyclic voltammogram of 0.1 mg/cm<sup>2</sup> MoS<sub>2</sub>, WS<sub>2</sub>, MoSe<sub>2</sub>, WSe<sub>2</sub>, MoTe<sub>2</sub> and WTe<sub>2</sub> respectively at scanning rates of 5, 10, 15, 20, 25, 50, 100, 125, 175, 200 and 250 mV/s and potential window of 0.1 to 0.3 V vs RHE. (H) Linear fitting of the capacitive currents of the 6 TMD films vs scan rates. The calculated double-layer capacitances are 1, 0.42, 0.36, 0.41, 0.45 and 0.41 mF/cm<sup>2</sup> for MoS<sub>2</sub>, WS<sub>2</sub>, MoSe<sub>2</sub>, WSe<sub>2</sub>, MoTe<sub>2</sub> and WTe<sub>2</sub> respectively.

### ***Electrochemical Impedance Spectroscopy of MoSe<sub>2</sub> and MoSe<sub>2</sub>/SWNT composite***

Electrochemical impedance spectroscopy was applied to characterize the HER reaction catalyzed by MoSe<sub>2</sub> nanosheets electrodes and study the effect of nanotube addition on HER mechanism. Figure show the Nyquist plots of two electrodes with the same mass loading (0.1 mg/cm<sup>2</sup>) with and without nanotubes. Both Nyquist plots contains two depressed semicircles which is quite common feature for HER on porous electrodes in acidic medium [1-3]. Each semi-circle is characterised by a single time constant (a constant phase element or non-ideal capacitor in parallel with a resistor). Although both types of films exhibit a similar general EIS response, characterised by two relaxation processes, distinct differences in their responses can be observed in high frequency as shown in Figure S- 17.

The data for both samples was fit with an equivalent electric circuit as in Figure S- 18 and the fitting parameters summarized in Table S-1 and S-2. For both electrodes, the electrolyte resistance  $R_{sol}$  is an overpotential independent Ohmic drop related to the electrical contact, wirings and electrolyte. The semicircle at lower frequencies is highly potential-dependent and represents the charge transfer process at the electrolyte-catalyst interface; thus,  $R_{ct}$  is the charge transfer resistance. The semicircle at higher frequencies represents a time constant that is due to large electronic resistance of the electrode (i.e. MoSe<sub>2</sub> or MoSe<sub>2</sub>/SWNT) so  $R_p$  is associated with the electrode resistance. It is known that, however the electron transport in a catalyst is a separate process from charge transfer reactions, it affects the global activity of the catalyst by affecting the Tafel slope [4-6]. Therefore one of the reasons that metallic TMDs exhibit tremendous HER activity, is the fast electron transport because of large electronic conductivity of this polymorph. The associated time constants ( $\tau_{ct} = R_{ct} \times C_{\phi}$ ) regarding the recombination or HER charge transport is largely decreased by increasing the overpotential for both electrodes and are nearly identical for both pure MoSe<sub>2</sub> and MoSe<sub>2</sub> composite film, showing no change in intrinsic catalytic activity of material. However except the zero potential, the electron transport time ( $\tau_p = R_p \times C_p$ ) in MoSe<sub>2</sub> composite film with 10 wt% SWNT is about twice as fast as the pure MoSe<sub>2</sub> film in all overpotential ranges, confirming that adding nanotube conductor improves HER activity of the films via facilitating electron transport within the nanosheet network. Therefore the addition of a good electronic conductor such as graphene or carbon nanotube accelerates the slow electron transport within the porous network of semiconducting TMD nanosheets and which will result in more active and scalable non-platinum TMD catalyst.

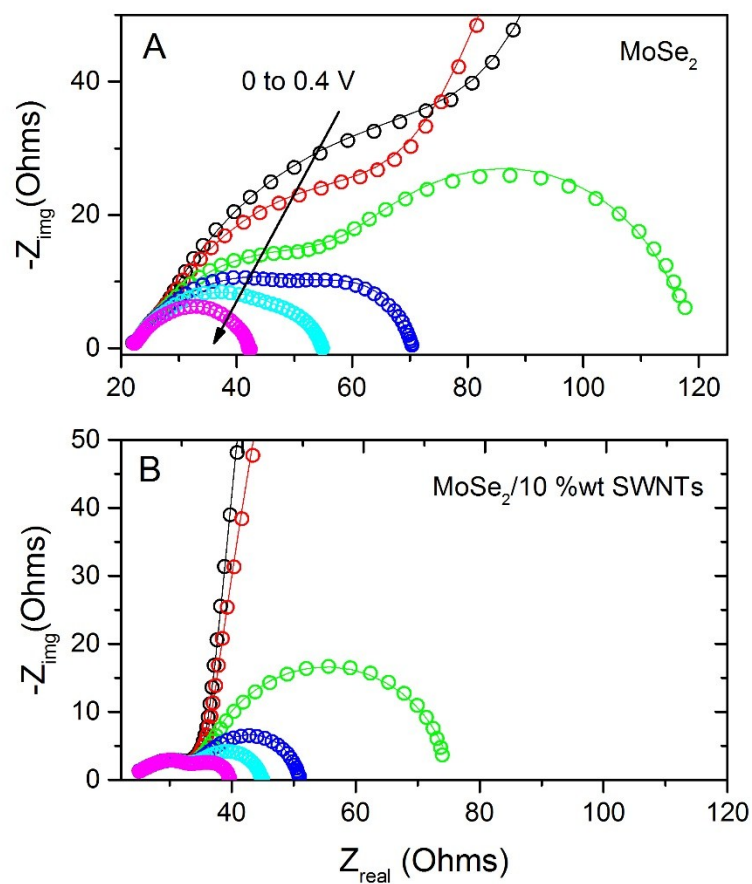


**Figure S- 17:** The Nyquist plot and fitting for the impedance response of 0.1 mg/cm<sup>2</sup> pure MoSe<sub>2</sub> film (A) and 0.1 mg/cm<sup>2</sup> MoSe<sub>2</sub> with 10wt% SWNT (B) at 0, 0.1, 0.2, 0.25, 0.3 and 0.4V overpotential

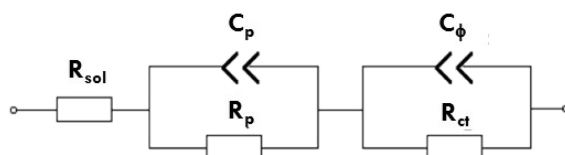


**Figure S- 18:** The equivalent circuit for the impedance data using two time constant model

**Table S-1:** fit parameters for 0.1 mg/cm<sup>2</sup> of MoSe<sub>2</sub> electrode

$\eta$ (mV)	$R_{sol}$ ( $\Omega$ )	$R_p$ ( $\Omega$ )	$C_p$ (mF/cm <sup>2</sup> )	$\tau(R_p \times C_p)$ Sec	$R_{ct}$ ( $\Omega$ )	$C_\phi$ (mF/cm <sup>2</sup> )	$\tau(R_{ct} \times C_\phi)$ Sec
0	22.08	84.25	0.87	0.073	2525	2.58	6.5
100	21.95	63.05	0.86	0.054	1352	2.659	3.6
200	21.94	46.53	0.92	0.043	50	3.926	0.20
250	21.94	38.46	0.89	0.034	11	6.823	0.075
300	21.94	30.41	0.75	0.023	2.8	13.22	0.036
400	21.83	19.7	0.57	0.011	2.1	11.13	0.023

**Table S-2:** fit parameters for 0.1 mg/cm<sup>2</sup> of MoSe<sub>2</sub> electrode with 10 wt% SWNTs

$\eta$ (mV)	$R_{sol}$ ( $\Omega$ )	$R_p$ ( $\Omega$ )	$C_p$ (mF/cm <sup>2</sup> )	$\tau(R_p \times C_p)$ Sec	$R_{ct}$ ( $\Omega$ )	$C_\phi$ (mF/cm <sup>2</sup> )	$\tau(R_{ct} \times C_\phi)$ Sec
0	23	19.88	15.9	0.317	2464	2.862	7.1
100	23	13.67	1.6	0.022	1317	4.105	5.4
200	24	13.23	1.53	0.020	40	4.874	0.20
250	23.32	13.53	1.37	0.019	12	6.001	0.07
300	23.53	9.595	0.52	0.005	10	4.786	0.048
400	23.52	10.76	0.59	0.006	4.4	4.268	0.019

## References

- [1] Navarro-Flores, Elisa, Zhiwen Chong, and Sasha Omanovic. "Characterization of Ni, NiMo, NiW and NiFe electroactive coatings as electrocatalysts for hydrogen evolution in an acidic medium." *Journal of Molecular Catalysis A: Chemical* 226.2 (2005): 179-197.
- [2] Kubisztal, J., A. Budniok, and A. Lasia. "Study of the hydrogen evolution reaction on nickel-based composite coatings containing molybdenum powder." *International Journal of Hydrogen Energy* 32.9 (2007): 1211-1218.
- [3] Kellenberger, Andrea, et al. "Kinetics of hydrogen evolution reaction on skeleton nickel and nickel–titanium electrodes obtained by thermal arc spraying technique." *International Journal of Hydrogen Energy* 32.15 (2007): 3258-3265.
- [4] Vrabel, Heron, et al. "Revealing and accelerating slow electron transport in amorphous molybdenum sulphide particles for hydrogen evolution reaction." *Chemical Communications* 49.79 (2013): 8985-8987.
- [5] Li, Yanguang, et al. "MoS<sub>2</sub> nanoparticles grown on graphene: an advanced catalyst for the hydrogen evolution reaction." *Journal of the American Chemical Society* 133.19 (2011): 7296-7299.

[6] Kim, Jaemyung, et al. "Enhanced electrocatalytic properties of transition-metal dichalcogenides sheets by spontaneous gold nanoparticle decoration." *The Journal of Physical Chemistry Letters* 4.8 (2013): 1227-1232.